Polarization Performance Simulation for the GeoXO Atmospheric Composition Instrument: NO_2 Retrieval Impacts

Aaron Pearlman[1,3], Monica Cook[1,3], Boryana Efremova[1,3], Francis Padula[1,3], Lok Lamsal[2,3], Joel McCorkel[3], and Joanna Joiner[3]

[1]GeoThinkTank LLC, Miami, FL, USA
[2]University of Maryland Baltimore County (UMBC), Baltimore, MD, USA
[3]NASA Goddard Space Flight Center, Greenbelt, MD, USA

Correspondence: Aaron Pearlman (aaron@geothinktank.com)

Abstract. NOAA's Geostationary Extended Observations (GeoXO) constellation will continue and expand on the capabilities of the current generation of geostationary satellite systems to support US weather, ocean, atmosphere, and climate operations. It is planned to consist of a dedicated atmospheric composition instrument (ACX) to support air quality forecasting and monitoring by providing similar capabilities to missions such as TEMPO (Tropospheric Emission: Monitoring Pollution), currently planned to launch in 2023, and OMI (Ozone Monitoring Instrument), TROPOMI (TROPOspheric Monitoring Instrument), and GEMS (Geostationary Environment Monitoring Spectrometer) currently in operation. As the early phases of ACX development are progressing, design trade-offs are being considered to understand the relationship between instrument design choices and trace gas retrieval impacts. Some of these choices will affect the instrument polarization sensitivity (PS), which can have radiometric impacts on environmental satellite observations. We conducted a study to investigate how such radiometric impacts can affect NO_2 retrievals by exploring their sensitivities to time of day, location, and scene type with an ACX instrument model that incorporates PS. The study addresses the basic steps of operational NO_2 retrievals: the spectral fitting step and the conversion of slant column to vertical column via the air mass factor (AMF). The spectral fitting step was performed by generating at-sensor radiance from a clear sky scene with a known NO_2 amount, the application of an instrument model including both instrument PS and noise, and a physical retrieval. The spectral fitting step was found to mitigate the impacts of instrument PS. The AMF-related step was considered for clear sky and partially cloudy scenes, where instrument PS can lead to errors in interpreting the cloud content, propagating to AMF errors and finally to NO_2 retrieval errors. For this step, the NO_2 retrieval impacts were small but non-negligible for high NO_2 amounts; we estimated that a typical high NO_2 amount can cause a maximum retrieval error of 0.25×10^{15} molecules/cm^2 for a PS of 5%. These simulation capabilities were designed to aid in the development of a GeoXO atmospheric composition instrument that will improve our ability to monitor and understand the Earth's atmosphere.

1 Introduction

NOAA's Geostationary Extended Observations (GeoXO) constellation will continue and expand on the capabilities of the current generation of geostationary satellite systems to support US weather, ocean, atmosphere, and climate operations. It is

planned to consist of a dedicated atmospheric composition instrument (ACX) to support air quality monitoring and forecast-
25 ing. The mission will build on knowledge obtained from low earth orbit (LEO) and geostationary (GEO) satellite air quality
monitoring instruments such as TROPOspheric Monitoring Instrument (TROPOMI) (Veefkind et al. (2012)), OMI (Ozone
Monitoring Instrument) (Levelt et al. (2006, 2018)), Geostationary Environment Monitoring Spectrometer (GEMS) (Kim et al.
(2020)), and Sentinel 4 (Kolm et al. (2017)). Retrievals of trace gases like NO_2 derived from satellite platform observations
have been used to relate top-down emissions estimates, air quality monitoring and forecasting, pollution events, trends, and
30 health studies (Bovensmann et al. (2011); Levelt et al. (2018); Burrows et al. (1999); Bovensmann et al. (1999); Levelt et al.
(2006); Munro et al. (2016); Bak et al. (2017); Veefkind et al. (2012); Cooper et al. (2022); Hollingsworth et al. (2008)). The
World Health Organization has designated NO_2 as a pollutant, since it has detrimental effects on human health (WHO (2021);
Huangfu and Atkinson (2020)). It also impacts climate by contributing to the formation of aerosols in the upper troposphere that
reflect incoming solar radiation, and, thus, cool the planet (Shindell et al. (2009). Over non-polluted regions, the stratospheric
35 NO_2 participates in photochemical reactions that can affect the ozone layer (Crutzen (1979)).

In the near future, these phenomena will be monitored from geostationary (GEO) orbit over the greater North America as
part of the TEMPO (Troposphere Emission: Monitoring Pollution) mission (Zoogman et al. (2017)), at an increased temporal
frequency than available from its LEO counterparts. Like other atmospheric composition monitoring instruments, TEMPO is
and ACX will be a hyperspectral imager with fine spectral sampling and resolution from the ultraviolet to the near-infrared
40 allowing trace gas absorption features to be discriminated using the well-known differential optical absorption spectroscopy
(DOAS) technique. For total vertical NO_2 amount retrievals, the DOAS technique is applied around the 420 to 455 nm range
(Bucsela et al. (2006); Lamsal et al. (2021); Marchenko et al. (2015); Boersma et al. (2007); Richter and Burrows (2002); Valks
et al. (2011); Martin (2002)).

ACX is in its early stages of development with its initial performance requirements being formulated with respect to param-
45 eters like sampling and resolution to enable this DOAS approach. Other parameters such as pixel size, noise, and polarization
sensitivity (PS) are also being defined. These requirements may be updated as the instrument design choices are better un-
derstood. This study focuses on the requirements for instrument PS, which, for instance, may inform whether a polarization
scrambler is needed. Air quality monitoring instruments such as OMI and TROPOMI were designed with polarization scram-
blers to reduce their PS (Bézy et al. (2017); Voors et al. (2017)).

50 Without PS suppression, the polarization state of incoming radiation will impact the at-sensor radiance for satellites sensors
in both GEO (Pearlman et al. (2015)) and LEO, though these impacts have been more extensively analyzed for LEO satellites
(Meister and Franz (2011); Wu et al. (2017); Goldin et al. (2019)). GEO orbit presents unique challenges due to the highly
variable solar angles throughout the day. This results in a variation in the degree of linear polarization of the at-sensor radiance
throughout the day due to Rayleigh scattering in the Earth's atmosphere; for instance, light scattered in the normal direction
55 to the incident light generates highly polarized radiation but not in the forward or backward direction. If the instrument is
sensitive to light with a certain polarization, this variation in degree of linear polarization translates to a variation in measured
radiance throughout the day. Thus, limiting the PS of the satellite sensor can limit the radiometric uncertainty. These impacts

can be derived by employing radiative transfer simulations to predict the at-sensor polarization state or Stokes parameters (S) and applying the instrument polarization impacts via its Mueller matrix ($\mathbf{M}$).

$$\begin{aligned}\mathbf{S} &= [\mathbf{S_0}\ \mathbf{S_1}\ \mathbf{S_2}\ \mathbf{S_3}]^{\mathbf{t}} \\ \mathbf{S'} &= \mathbf{M}\,\mathbf{S}\end{aligned} \tag{1}$$

The Stokes formulation expresses the polarization state consisting of its un-polarized (or randomly polarized) component, S_0; two terms describe its linear polarization state: the excess in horizontal linear polarization relative to the vertical direction, S_1, and excess in linear polarization at 45° relative to 135°, S_2; one term describing its circular polarization through its excess of right circular relative to left circular polarization, S_3. The Mueller matrix is a 4 x 4 matrix used to apply the optical effects of an element to generate an output Stokes vector. We model ACX as a Mueller matrix with a transmission of one and non-zero linear polarization extinction elements (m_{01}, m_{02}, m_{10}, and m_{20}). Since the system only detects total energy or radiance, not polarization state, only the first row is relevant. So the output term corresponding to the detected normalized Stokes parameter is:

$$S'_{ACX} = 1 + m_{01}S_1 + m_{02}S_2 \tag{2}$$

This detected radiance can differ from the true at-sensor radiance if ACX has linear PS, defined as $\sqrt{(m_{01}^2 + m_{02}^2)}$, which can propagate to higher level satellite products. For instance, the retrieval of surface reflectance can suffer large uncertainties, especially when the signal from the surface is small compared to the atmospheric component. In this work, we discuss our study of NO_2 retrievals, and investigate the parts of the process that may be affected. To our knowledge, NO_2 retrievals dependence on instrument PS have not yet been fully documented. We describe an initial study to show the ways that these retrievals can be impacted and make initial estimates of those impacts associated with the current PS requirements, <5% PS for wavelengths <500 nm.

Our NO_2 retrieval simulation approach discussed here follows a simplified version of the DOAS technique used for operational NO_2 retrievals and consists of two basic steps: One involves the DOAS spectral fitting step for the at-sensor radiance. This fit is normally used to retrieve the NO_2 slant column amount —the total number of molecules along the atmospheric photon path to the satellite sensor. The second step converts this slant column amount to the vertical column amount through the air mass factor (AMF), which depends on the geometrical path as well as the differences in scattering and absorption within the atmosphere between the slant and vertical paths. Our first approach for analyzing polarization effects deals with the DOAS spectral fitting step with clear sky scenes by simulating at-sensor Stokes parameters and applying an instrument model that includes a range of PS values in several orientations (defined by m_{01} and m_{02}), as well as the instrument noise and spectral properties consistent with our current knowledge of ACX. The fits of these spectra are used to retrieve NO_2 vertical column amount directly, not slant column, in our case; since these are simulations with the vertical profiles used as inputs, we do not need to use the AMF for converting slant column to vertical column amount. The second approach deals exclusively with the AMF derivation step. For this analysis, the AMF, required for operational retrievals, is affected by instrument PS when

considering the potential for partially cloudy scenes. Retrievals in such situations are commonly performed for atmospheric
90   monitoring instruments, since their large instantaneous fields of view make completely clear scenes rare. We will discuss the
formalism in detail for both approaches in the methods section. With these two approaches, referred to as the method for "clear
scenes" and "partially cloudy scenes", we demonstrate the capability to investigate PS requirements.

2   Methods

As mentioned, the approach for clear scenes exploits the spectral features in the radiance spectra to retrieve the total vertical
95   amount of NO_2, and the approach for cloudy scenes relies on the AMF calculation.

2.1   Clear scenes

The overall method for clear scenes is illustrated in Fig. 1. In this process, simulated radiance spectra are propagated through
an instrument model and the total vertical column NO_2 is retrieved using a look-up table (LUT) approach with the aid of a
constrained energy minimization algorithm (CEM) algorithm (Farrand (1997)). Further details are discussed below.
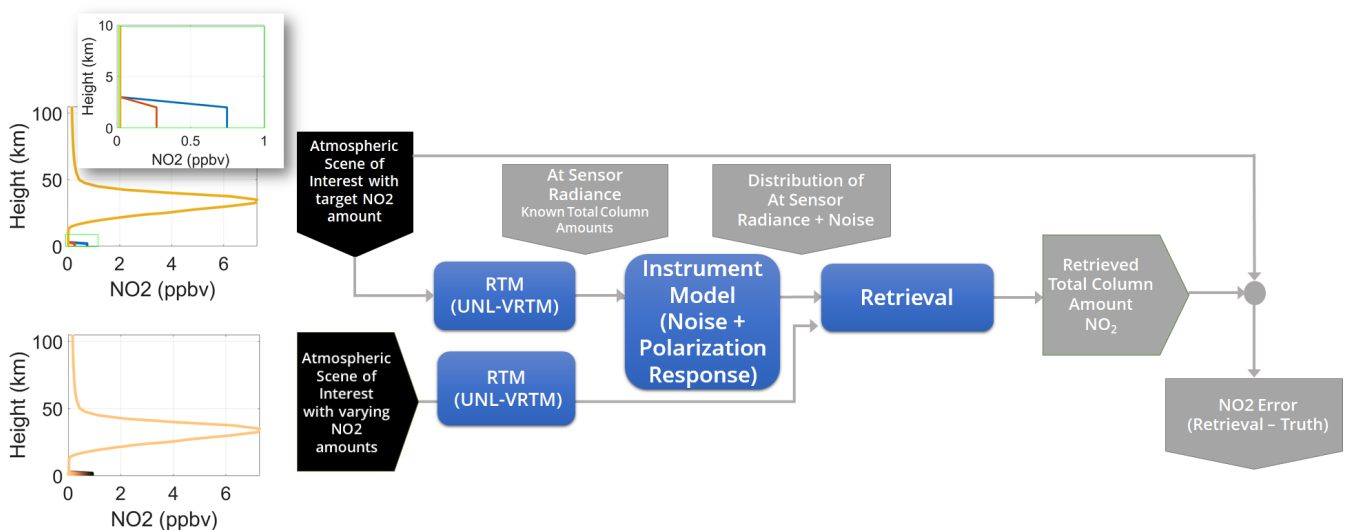

Figure 1. Simulation method for retrieving NO_2 in clear scenes: The scenes of interest consist of selected custom NO_2 profiles to represent
low, medium, and high NO_2 cases shown at the upper left (including a zoomed-in view) corresponding to total vertical NO_2 amounts of
$4.60, 5.93,$ and 8.44×10^{15} molecules/cm^2, respectively. The lower left profiles contain all profiles used in the retrieval process. The profiles
are used in the radiative transfer model (RTM) called the Unified Linearized Vector Radiative Transfer Model (UNL-VRTM) to generate
at-sensor radiance.

4

2.1.1 Radiative Transfer Modeling

The at-sensor radiances from clear scenes are simulated using a vector radiative transfer code, the Unified Linearized Vector Radiative Transfer Model, UNL-VRTM, which integrates the linearized vector radiative transfer (VLIDORT) into a broader framework (Xu and Wang (2019)). The code can generate Stokes vectors from any scene defined by its view and solar geometry, surface reflectance, wavelength range, and atmospheric composition. Note that rotational Raman scattering is not included in the model. The ACX was assumed to be at 105° West longitude viewing several locations across the continental US (CONUS). The time of day was chosen to generate solar zenith angles of 60 to 70°, where PS is expected to be highest but still within the range where NO_2 retrievals are typically performed. The US Standard Model default profiles were used for 21 trace gases for all scenes (excluding NO_2). The default NO_2 profiles were modified by injecting a known amount uniformly into the troposphere below 2 km (Fig. 1). Three basic surface spectra generated from spectral libraries were used. The water spectrum used is associated with an open ocean case (Kokaly et al. (2017)); the vegetation is a combination of trees (30 %), grass (30 %), shrubs (30 %), non-photosynthetic material (5 %), and soil (5 %), and the urban case is a combination of roof (50 %), concrete (20 %), road (20 %), and vegetation (10 %) (Meerdink et al. (2019); Baldridge et al. (2009)) as depicted in Fig. 2. Their associated background aerosol content was included in the boundary layer up to 2 km with a uniform vertical distribution. The rural and urban scenes use a bi-modal aerosol distribution as shown in Table 1, where the loading and size distribution values for each mode are given for these scenes. The aerosol parameters including the complex indices of refraction per wavelength were taken from Shettle et al. (1979) (with mean values listed in the Table) and aerosol optical depth (AOD) values from the climatology reported in Yan et al. (2021).
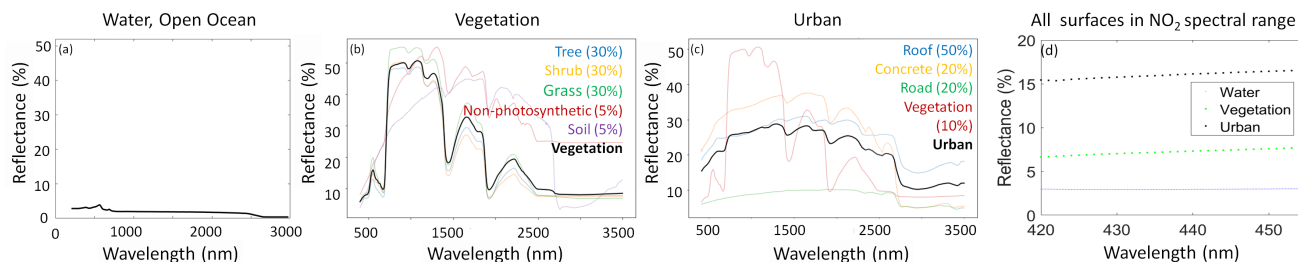

Figure 2. Basic surfaces reflectance spectra used in radiative transfer simulations: (a) water, (b) vegetation and (c) urban. (d) Spectra in the NO_2 retrieval spectral range.

We ran radiative transfer simulations for several US locations, with the three scene types, with varying amounts of tropospheric NO_2. This produced a look up table (LUT) of scene type, NO_2 vertical amount, and at-sensor radiance spectra. This LUT was used in the retrieval discussed below.

5

Table 1. UNL-VRTM Parameters

Scene	Reflectance Spectrum	Type(s)	Index of refraction		AOD [1]	Size distribution	
			Real	Imaginary		$\bar{r}$ [μm] [2]	σ_r [μm] [3]
Water	Open ocean	Sea Salt	1.50	0.0	0.08	0.3	0.4
Rural	Trees	Water soluble	1.53	0.0050	0.13	0.03	0.35
	Shrubs	Dust	1.53	0.0049	0.42	0.5	0.4
	Grass						
	Non-photosynthetic						
	Soil						
Urban	Roof	Water soluble	1.53	0.0050	0.03	0.03	0.35
	Concrete	Soot	1.75	0.456	0.5	0.5	0.40
	Road						
	Vegetation						

[1] aerosol optical depth

[2] radius mean

[3] radius standard deviation

2.1.2 Instrument model and NO_2 retrievals

The reference radiance spectra corresponding to the NO_2 reference amounts over water, rural and urban scenes were modified by applying the instrument model (for several US locations). The instrument response model was based on the TEMPO design, which consists of of a reflective f/3 Schmidt-form telescope and a spectrometer assembly that utilizes a diffraction grating
125 to form an image on CCD detector arrays (Zoogman et al. (2017)). The simulated radiance was modified by this instrument response model, which sampled the radiance at 0.2 nm wavelength steps with a resolution of 0.6 nm, and applied a PS response. The PS response model was not specific to TEMPO as our goal was to understand the range of impacts associated with the ACX polarization requirements. The noise was also applied as defined by the ACX signal-to-noise (SNR) specification. Our instrument parameters from TEMPO were modified by assuming a sampling strategy or integration time modification that
130 brought the noise in line with that specified by ACX. Table 3 shows the parameters included in this model.

Table 2. ACX instrument response model parameters

Parameter	Description
$L(\lambda)$	Spectral radiance at instrument resolution
A_{det}	Detector area
$\Omega = \pi/4(f\#)^2$	Solid angle of acceptance
Δt	Integration time
λ	Wavelength
$\Delta\lambda$	Spectral interval per pixel
$\tau(\lambda)$	Optical system transmittance combined with grating efficiency
$\eta(\lambda)$	Detector quantum efficiency
N	Bit depth
n_{read}	Read noise
I_{dark}	Dark current

The noise was applied by generating 1000 spectra with different amounts of noise following a Gaussian distribution that are added to the at-sensor radiance (after being modified by the polarization response). All spectra were normalized by subtracting a second order polynomial fit to remove the sensitivity to absolute radiance as is done in the DOAS retrieval technique. The NO_2 vertical amount was retrieved using the look-up-table and the CEM algorithm:

$$CEM = \frac{(t-m)^T C^{-1}(x-m)}{(t-m)^T C^{-1}(t-m)}, \tag{3}$$

135

where C^{-1} and m are the inverse covariance matrix and mean over the noise spectra, respectively. The CEM was calculated for all (target) spectra in the LUT, t, with the noise spectra, C^{-1} and m. The spectrum, x that generated a CEM value closest to one was chosen, and its associated NO_2 vertical amount was retrieved.

2.2 Partially cloudy scenes

140 The process for "partially cloudy scenes" involves an AMF derivation process that includes the consideration of subpixel-scale clouds. The typical instantaneous field of view for an atmospheric composition instruments means that most scenes contain some clouds. Operational trace gas retrievals are routinely done in partially cloudy scenes, so we derive PS impacts for such scenes primarily through their impact on the AMF.

2.2.1 Theoretical background

145 This approach assumes a simple cloudy scene model where each scene is assumed to be a combination of a fully cloud covered subpixel and a clear sky subpixel weighted with an effective cloud fraction, f, consistent with previous approaches (Stammes et al. (2008)):

$$L_{obs} = L_{clr}(1-f) + L_{cld}f, \tag{4}$$

where L_{obs} is the observed radiance, L_{clr} is the calculated radiance in a clear sky, and L_{cld} is the cloudy radiance. To produce
150 observed amounts of Rayleigh scattering and absorption, it was found that for this equation to work across most conditions, we model L_{cld} as a Lambertian surface (opaque) with surface reflectivity 0.80 at the effective cloud pressure, assumed here to be equivalent to a cloud at 2 km. Aerosols are not considered for the cloudy scenes, since they would have a negligible impact; the clouds would lie above the tropospheric NO2 and aerosol layer. This simple model has been demonstrated to represent the complex radiative transfer in clouds accurately (Stammes et al. (2008); Joiner (2004); Vasilkov et al. (2008)). So, we typically
155 derive f at a wavelength with little absorption and use a surface climatology for L_{clr}. Then, we simply invert the above equation to give:

$$f = \frac{L_{obs} - L_{clr}}{L_{cld} - L_{clr}}. \tag{5}$$

For the trace gas retrievals, another quantity defines the fraction of scene radiance from the cloud versus the clear parts of the scene called the cloud radiance fraction, f_r, which has wavelength dependence:

$$f_r = f \frac{L_{cld}}{L_{obs}}. \tag{6}$$

A cloudy air mass factor (AMF) is computed along with the clear sky AMF. The total AMF is then computed with the clear and cloudy AMFs weighted by the cloud radiance fraction

$$\text{AMF}_{total} = \text{AMF}_{clr}(1 - f_r) + \text{AMF}_{cld}f_r. \tag{7}$$

To compute the error in the NO_2 vertical column due to an error in f, we started with the calculation of the error in f due to an error from PS:

$$\frac{df}{d\epsilon_{PS}} = \frac{dL_{obs}}{d\epsilon_{PS}} \frac{1}{(L_{cld} - L_{clr})}, \tag{8}$$

and this would then propagate into the error in NO_2 vertical column density ($NO_{2,VCD}$) through Equations 6,7 above along with:

$$NO_{2,\text{VCD}} = \frac{NO_{2,\text{SCD}}}{\text{AMF}_{total}}. \tag{9}$$

This process is shown graphically in Fig 3, where a clear and cloudy version of a scene are simulated. The clear version is propagated through the instrument polarization response model, and, using the radiance generated from the cloudy scene, the impacts are propagated through the cloud fraction, cloud radiance fraction, AMF, and finally the NO_2 amount. Following the process by Kuhlmann et al. (2015), the AMFs for each atmospheric layer (also called box AMFs) were computed using a pre-calculated LUT with input parameters of altitude, z, solar zenith angle, view zenith angle, relative azimuth angle, surface reflectance, and surface altitude. The total AMF was calculated by linearly interpolating over all variables for each altitude and summing over all layers to the top of atmosphere (TOA), where each layer dz has a vertical column amount V_{NO_2}:

$$\text{AMF}_{clr/cld} = \frac{\int_0^{TOA} \alpha \cdot \text{AMF(z)} \cdot V_{NO_2} dz}{\int_0^{TOA} V_{NO_2} dz}, \tag{10}$$

where the integration assumes an exponential dependence within each layer. A correction term, α, is normally included in the AMF calculation to account for the temperature dependence of the NO_2 cross sections, though was neglected here by setting it to one. The NO_2 error derived through the conversion of slant to vertical amount is then computed. This error can be considered as the effect of a change in detected radiance due to PS, which, in turn, leads to an error in the interpretation of the amount of clouds in the scene. This leads to an impact on the NO_2 retrieval over the total vertical column. Note that assuming a constant PS over the wavelength range, this error will also change negligibly as a function of wavelength. We perform this

8

analysis at one wavelength (425.8 nm) in this study. By differentiating Equation 9, the NO_2 error in the total vertical column amount ($\partial(NO_{2,total})$) is then calculated in terms of the total vertical NO_2 amount ($V_{NO_2,total}$), the AMF, and the AMF error (∂AMF_{total}) as:

$$\partial(NO_{2,total}) = \frac{-V_{NO_2,total}}{AMF_{total}} \cdot \partial(AMF_{total}).$$

(11)

2.2.2 Radiative transfer modeling

We conducted the radiative transfer simulations as summarized in Table 3. Simulation A will be shown to define an upper bound for the retrieval error with a PS of 5% by using a NO_2 profile (similar to those defined in the clear scene simulations) with a large NO_2 amount, the lowest reflectance scene, and high constant solar zenith angle over all of CONUS over a one degree latitude/longitude grid. Simulation B quantifies the retrieval impact of scene type —water, rural, and urban scene —over CONUS for a constant reference NO_2 profile. The scene types are the same as defined in Table 1 and are assigned to all pixels in CONUS for each run. Simulation C explores the retrieval impacts on the solar zenith angle and NO_2 amount for selected US locations. The PS is also varied over a wider range of values. Finally, Simulation D uses NO_2 profiles from the Goddard Earth Observing System Model, Version 5 (GEOS-5) (Molod et al. (2012)) on a particular time and day with a fixed scene type over the CONUS grid. Simulations A-C give a contrived version that is useful for bounding the impacts of instrument PS and isolating impacts of different variables. Simulation D represents cases with more realistic nominal parameters. Note that we also used the cloud fraction from the GEOS-5 model for deriving the simulated radiance prior to applying the polarization response model. This deviates from the illustration in Fig. 1 (top left), where instead of a clear scene, a mixture of cloudy and clear scene according to the GEOS-5 cloud fraction value is used, thereby accounting for the radiance polarization state of both clear and cloudy scenes in generating the NO_2 retrieval errors. A single day was chosen to demonstrate this approach, July 15, 2007 on two selected times 16 UTC and 20 UTC, so that the impacts of extreme solar zenith angles (corresponding to high degree of linear polarization) could be seen for both the eastern and western US regions.

Table 3. ACX Radiative Transfer Simulation for Cloudy Scenes

Simulation	NO$_2$ amount	Solar zenith angle/Time	Scene	Polarization Sensitivity (PS)	Orientation	Locations
A	20×10^{15} molecules/cm^2	70°	Water	5 %	Vertical	CONUS[1]
					45°	
B	8.4×10^{15} molecules/cm^2	70°	Water	5 %	Vertical	CONUS
			Vegetation			
			Urban			
C	20×10^{15} molecules/cm^2	70°	Water	Variable	Vertical	Select locations
	8.4×10^{15} molecules/cm^2	30°			Horizontal	
	5.9×10^{15} molecules/cm^2					
D	GEOS-5[2] profiles	16 UTC	Water	5%	Vertical	CONUS
		20 UTC				

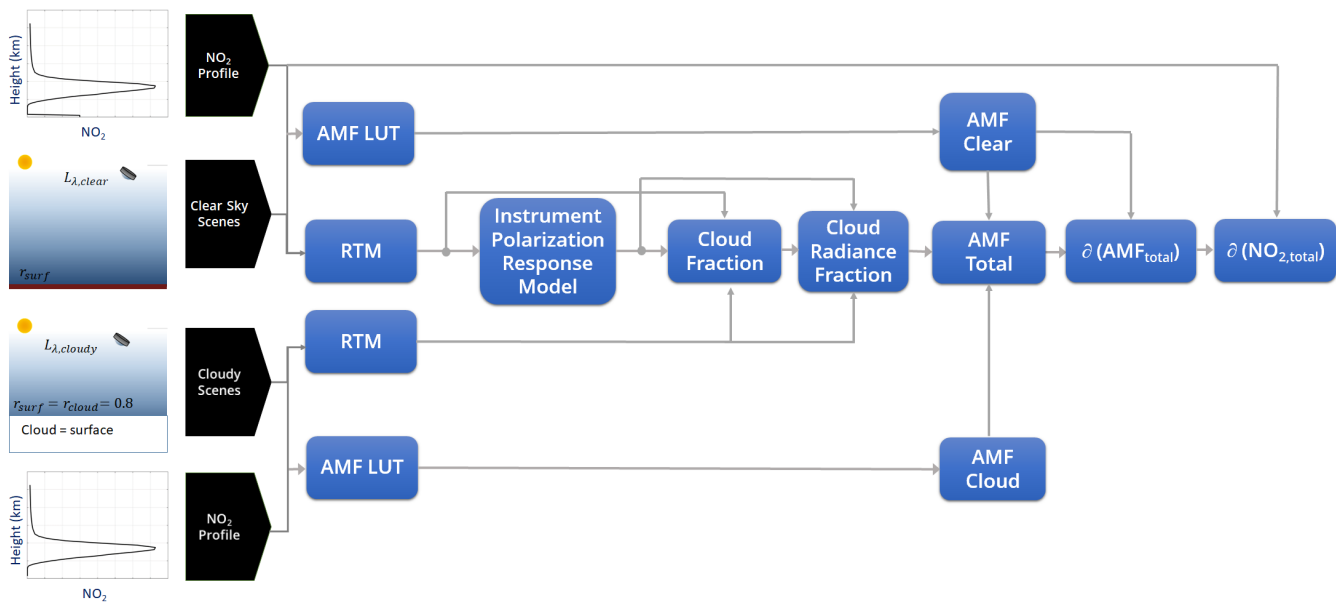1 Continental United States, 2 Goddard Earth Observing System Model, Version 5

Figure 3. Simulation method for deriving NO_2 errors by interpreting a clear scene as a partially cloudy scene due to instrument PS: Through radiative transfer modeling (RTM) and air mass factor (AMF) calculations via a look-up table (LUT) of clear and cloudy scenes, and applying the instrument polarization response model to a clear scene, the NO_2 error is determined by propagating through the variables shown to errors in AMF ($\partial(AMF_{total})$) and total vertical NO_2 amount ($\partial(NO_{2,total})$)

3 Results

3.1 Clear scenes

As part of the method for clear scenes, the ACX instrument model was applied to the at-sensor radiance including sampling with a Gaussian slit function at the interval and resolution of 0.2 and 0.6 nm, respectively, and its noise as depicted in Fig. 4. The differences between the normalized solar irradiance (multiplied by a factor of 5 for visibility) and radiance spectra shows the atmospheric contribution and the effects of this resampling. The 1000 radiance spectra shown cannot be discerned clearly given the high SNR (explicitly shown by the blue line). The noise was applied after modifying with the PS response. The PS model parameters applied via Equation 2 using $m_{01} = \pm PS$ and $m_{02} = 0$, so that the PS was applied in the vertical or horizontal orientation. These orientations were chosen for most simulations for simplicity but other orientations will be discussed in the cloudy scene analysis section.
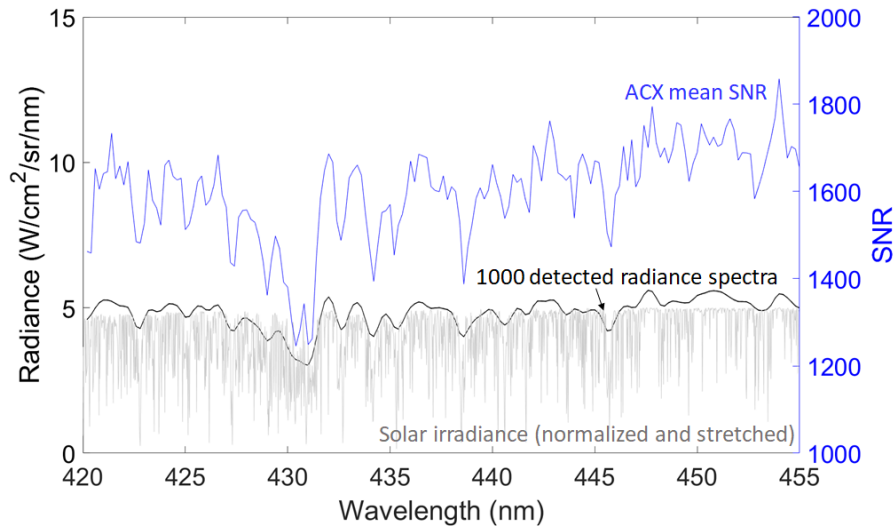
Figure 4. Example of at-sensor radiance spectra simulated with an applied instrument model including resampling effects and added noise set by ACX instrument parameters. 1000 spectra are plotted (black lines), which appears as a slightly thicker line than the mean SNR (blue line and right axis). The normalized solar irradiance multiplied by a factor of 5 is shown for comparison to the resampled spectra.

215   The retrieval process effectively matches the spectral shape of the simulated detected spectra —affected by spectral sampling, noise, and PS —to the most similar spectra in the LUT that contains a large range of tropospheric NO_2 amounts for the three surfaces. Figure 5(a) shows an example of a the adjusted sample spectrum with the the spectra in the LUT. Note that all spectra were adjusted using quadratic fits in the spectral fitting process. The CEM algorithm finds the spectrum from the spectra that is most similar. Figure 5(b) shows a summary of the NO_2 retrieval errors, average biases and standard deviations as a function of

220   PS for several scene types for a particular location (Norman, Oklahoma). The errors are driven by a combination of the SNR, view/solar geometry, surface reflectance spectrum, and aerosol model and are similar for all scene types. The flat dependence indicates that the PS does not affect the retrieval error in the DOAS spectral fitting retrieval step. The reason is that the PS is a smooth function of wavelength, and the radiometric error introduced are compensated through the spectral fitting process. These results were similar for all locations (not shown). We note that other retrieval techniques that do not use a polynomial

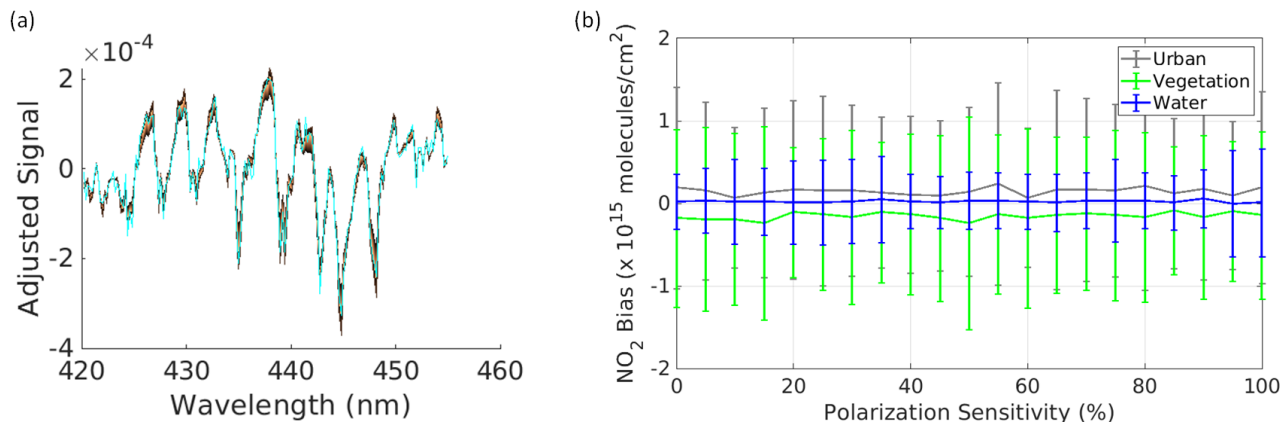225   correction term in the spectral fitting approach may exhibit larger PS impacts.

Figure 5. Clear-sky scene retrieval results: (a) An example of an adjusted ACX simulated spectrum (cyan) with all spectra from the look-up-table (LUT) with varying amounts of tropospheric NO_2 (b) The average error (or bias) and standard deviation for 1000 total vertical NO_2 retrievals of the "high" amount (8.44×10^{15} molecules/cm^2) for the three scene types (water, vegetation, and urban) at Norman, Oklahoma, assuming a vertical PS orientation.

3.2 Partially cloudy scenes

In contrast to the previous results, the AMF-related processing step showed more significant polarization impacts, where an error is induced when a clear scene scene is interpreted as a partially cloudy scene due to the instrument response model that includes PS (but not noise). Figure 6 shows the results as they are propagated through each step in the process (Fig. 3) for an example with an extremely high total vertical NO_2 amount, 20×10^{15} molecules/cm^2, over all of CONUS (Table 3, Simulation A). The simulation ran using $70°$ solar zenith angle and water scene for all pixels and an instrument PS of 5%, $m_{01} = -0.05$, vertical orientation and $m_{02} = 0.05$, $45°$ orientation, and an initial cloud fraction of zero. The Stokes parameter, S_1 is relevant for vertical (or horizontal) polarization and S_2 is relevant for $45°$ (or $135°$) polarization. The correlation between the relevant Stokes parameters, retrieved cloud fraction, and NO_2 error are particularly apparent. This example shows that the PS orientation can generate vastly different spatial dependence in NO_2 retrieval errors. The maximum NO_2 error of 1.4×10^{15} molecules/cm^2 is above the specified TEMPO NO_2 precision (Zoogman et al. (2017)). Note that this is likely an upper bound, since NO_2 amounts like these are mostly found in industrialized areas in other regions of the world.

Similar simulations for more realistic NO_2 amounts using constant profiles across CONUS show how these retrieval errors change as a function of surface type (Table 3, Simulation B). Figure 7 shows a lower, more realistic, NO_2 amounts of 8.4×10^{15} molecules/cm^2 corresponding to the "high" NO_2 case shown in Fig. 1. The results are shown for the three different scene types applied uniformly across all of CONUS. The other parameters are the same as the previous higher NO_2 case. The NO_2 error increases as the surface reflectance decreases. All cases show the same spatial pattern over CONUS as in the previous case. The maximum NO_2 error is 0.25×10^{15} molecules/cm^2.
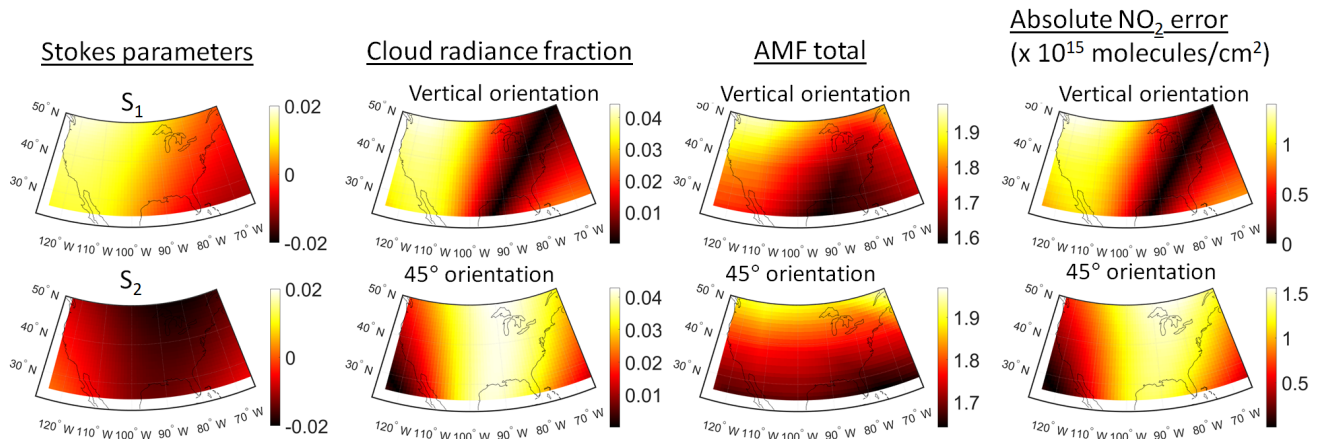
12

Figure 6. Derived parameters for NO_2 amount of 20×10^{15} molecules/cm^2 , water scenes, and 5% PS in a vertical and 45° orientation. (See Table 3, Simulation A for more details).
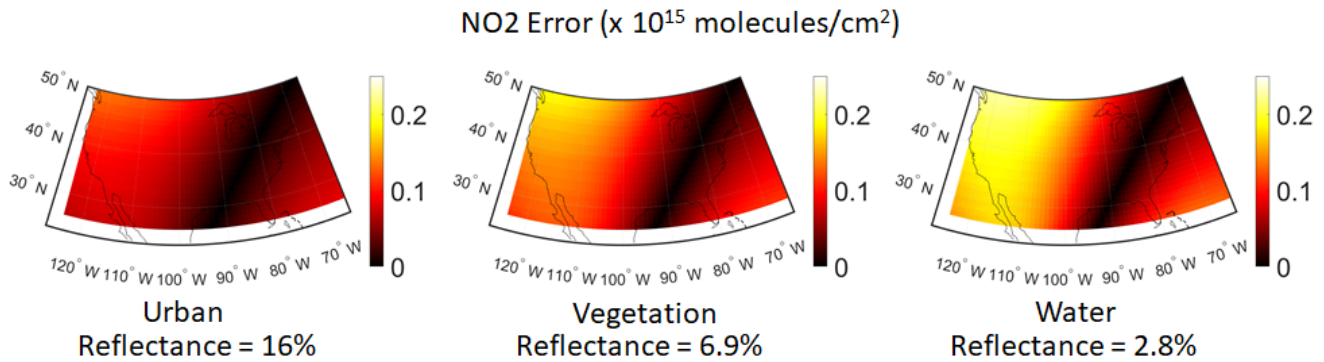

Figure 7. NO_2 errors assuming different scene types across CONUS for 5% PS in a vertical orientation and constant NO_2 profiles with 8.4 $\times 10^{15}$ molecules/cm^2. (See Table 3, Simulation B for more details).

Fig. 8 shows the results repeating similar simulations with different NO_2 amounts and times of day for select US locations

245 and their (non-linear) dependence on PS (Table 3, Simulation C). The figure shows that NO_2 errors derived decrease as the NO_2 amounts decrease using three different total vertical amounts: 5.9, 8.4, and 20×10^{15} molecules/cm^2 as a function of PS and two different orientations. The dependence on NO_2 amount is non-linear; for instance, at 5 % PS for the Seattle, evening case, the retrieval errors for increasing amounts are 0.22 %, 2.6 %, and 6.6 %. The time of day dependence is illustrated by the edge of the shading: the darker shading shows the retrieved NO_2 amount with a solar zenith angle of 30° and the edge

250 of the lighter shading shows the amount with an angle of 70°. The shading is meant to emphasize the difference between the reference and retrieved amount. The horizontal orientation results are similar to those for the vertical orientation. As evident in

the previous results, the largest NO_2 errors occur in the western regions (Seattle, San Diego) for these orientations. The lower solar zenith angle corresponds to lower linear degree of linear polarization, accounting for the lower NO_2 errors.
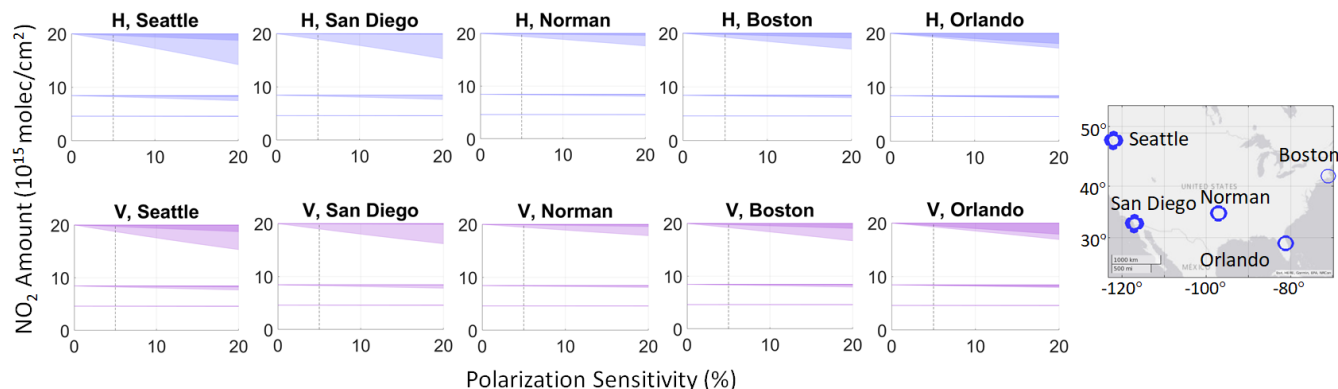

Figure 8. (Left) The retrieved amount is shown as a function of polarization sensitivity (PS) for two different orientations (H - horizontal, V - vertical) for selected US locations and NO_2 total vertical amounts: 5.0, 8.6, and 20×10^{15} molecules/cm^2. The edge of the darker (lighter) shading shows the retrieved NO_2 amount with a solar zenith angle of $30°$ ($70°$). The vertical dotted line shows the current PS requirement for reference. (Right) The locations are shown on the map with thicker circles representing higher NO_2 errors. (See Table 3, Simulation C for more details)

In contrast to the previous results with constant profiles across CONUS, Fig. 9 shows the results using GEOS-5 profiles,
255 which appear qualitatively consistent with the results using the artificial profiles used above (Table 3, Simulation D). The NO_2 amounts for this day varied between 2.5 to 6.5×10^{15} molecules/cm^2 are displayed . The figure shows the polarization impacts with 5% PS in the vertical orientation. The impacts are more apparent as the solar zenith angle increases and resemble the previous results in Fig. 7, where the solar zenith angle is fixed at 70 °. For instance, the NO_2 errors are larger at 20 UTC in the eastern regions where the solar angles are relatively large, and the NO_2 errors are larger in the western regions at UTC
260 16, where the solar zenith angles are larger. The higher cloud fraction decrease the retrieval errors, which can be seen in the western regions at 16 UTC; although the southwest and southeast have similar solar zenith angles, the southwest has lower retrieval errors due to the increased cloud fraction. As a result of the cloud fraction and lower NO_2 amount, the maximum NO_2 errors found were 0.03×10^{15} molecules/cm^2 for this day —a negligible value when compared to the TEMPO precision requirement.
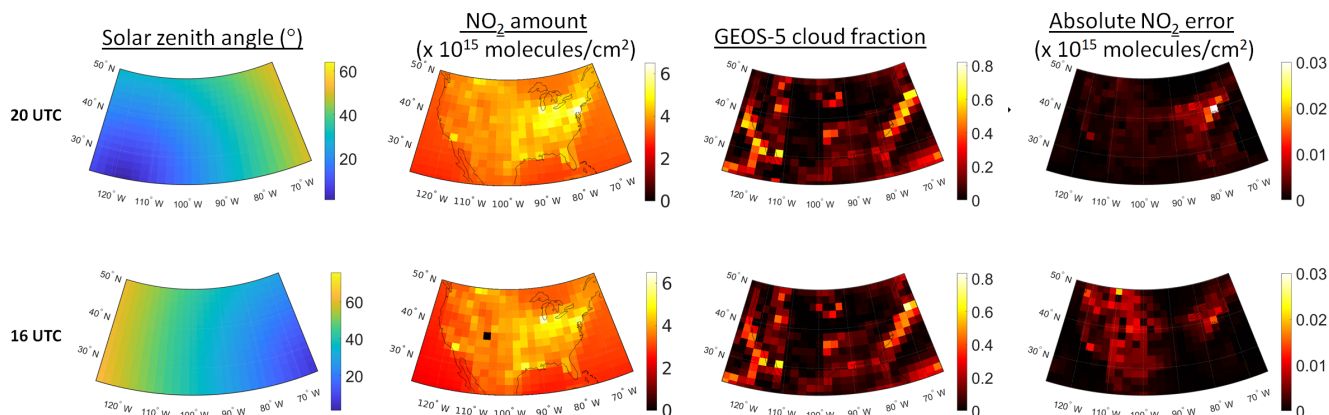
Figure 9. Solar zenith angles, total NO$_2$ column amount, GOES-5 cloud fraction, and resulting NO$_2$ errors at 20 UTC (top) and 16 UTC (bottom). GEOS-5 NO$_2$ profiles were used assuming 5% PS with vertical orientation, all water scenes, and clouds at a 2 km altitude. (See Table 3, Simulation D for more details)

4 Summary and conclusions

We demonstrated a simulation and modeling capability to assess polarization effects for ACX predicted performance studies. Our results show that the DOAS spectral fitting step mitigates PS effects in the NO$_2$ retrieval process. The AMF calculation step, however, can cause retrieval errors from instrument PS when considering partially cloudy scenes. The PS magnitude and orientation (Mueller matrix elements) impacts can cause different NO$_2$ retrieval errors depending on location, time of day, cloud fraction, and NO$_2$ amount. For a PS of 5 % with vertical orientation, the maximum NO$_2$ retrievals errors were 0.25×10^{15} molecules/cm^2 for high pollution cases. In extreme cases, if NO$_2$ pollution significantly increases to levels on the order of the world's most polluted regions, these errors can reach 1.4×10^{15} molecules/cm^2. A more typical maximum error found through analyzing the GEOS-5 profiles was 0.03×10^{15} molecules/cm^2. This study shows that in most cases, the 5% PS requirement introduces retrieval uncertainties significantly lower than the TEMPO precision requirement except in the most extreme cases. Note that these estimates assume a particular set of instrument Mueller matrix elements. We emphasized a vertical orientation based on an assumed vertical grating orientation where its polarization axis would likely be in this direction. In this configuration, the instrument effectively sweeps wavelengths over locations in the west-east direction. The Mueller matrix will be updated with the appropriate values as the instrument design matures to refine the estimates of NO$_2$ retrieval impacts. Our simplified retrieval approach may have neglected factors used in operational retrievals that could be affected by instrument PS and contribute to additional retrieval errors related to estimates of aerosols, surface reflectance, and cloud parameters. Rotational Raman scattering, which has been used in cloud height retrievals (e.g., Vasilkov et al. (2008)), for instance, can be particularly sensitive to polarization. Other approaches for cloud height retrievals such as oxygen dimer absorption (Acarreta et al. (2004)) should be much less sensitive. We do not account for the PS to cloud height retrievals. The PS to cloud optical thickness is implicitly accounted for within the effective cloud fraction estimation. In addition, the limited

set of surface reflectance types that were used and the directional and polarization surface effects that were neglected, can be included in future work to improve the accuracy of the results. This capability can be utilized to support the development of ACX to continue and build on the legacy of atmospheric composition measurements to forecast and monitor air quality.

References

WHO global air quality guidelines particulate matter (PM2.5 and PM10), ozone, nitrogen dioxide, sulfur dioxide and carbon monoxide, WHO European Centre for Environment and Health, Bonn, Germany, 2021.

Acarreta, J. R., Haan, J. F. D., and Stammes, P.: Cloud pressure retrieval using the $O_2 - O_2$ absorption band at 477 nm, Journal of Geophysical Research, 109, https://doi.org/10.1029/2003jd003915, 2004.

Bak, J., Liu, X., Kim, J.-H., Haffner, D. P., Chance, K., Yang, K., and Sun, K.: Characterization and correction of OMPS nadir mapper measurements for ozone profile retrievals, Atmospheric Measurement Techniques, 10, 4373–4388, https://doi.org/10.5194/amt-10-4373-2017, 2017.

Baldridge, A., Hook, S., Grove, C., and Rivera, G.: The ASTER spectral library version 2.0, Remote Sensing of Environment, 113, 711–715, https://doi.org/10.1016/j.rse.2008.11.007, 2009.

Bézy, J.-L., Bazalgette, G., Sierk, B., Meynart, R., Caron, J. C., Richert, M., and Loiseaux, D.: Polarization scramblers in Earth observing spectrometers: lessons learned from Sentinel-4 and 5 phases A/B1, in: International Conference on Space Optics — ICSO 2012, edited by Armandillo, E., Karafolas, N., and Cugny, B., SPIE, https://doi.org/10.1117/12.2309044, 2017.

Boersma, K. F., Eskes, H. J., Veefkind, J. P., Brinksma, E. J., van der A, R. J., Sneep, M., van den Oord, G. H. J., Levelt, P. F., Stammes, P., Gleason, J. F., and Bucsela, E. J.: Near-real time retrieval of tropospheric NO_2 from OMI, Atmospheric Chemistry and Physics, 7, 2103–2118, https://doi.org/10.5194/acp-7-2103-2007, 2007.

Bovensmann, H., Burrows, J. P., Buchwitz, M., Frerick, J., Noël, S., Rozanov, V. V., Chance, K. V., and Goede, A. P. H.: SCIA-MACHY: Mission objectives and measurement modes, Journal of the Atmospheric Sciences, 56, 127 – 150, https://doi.org/10.1175/1520-0469(1999)056<0127:SMOAMM>2.0.CO;2, 1999.

Bovensmann, H., Aben, I., Van Roozendael, M., Kühl, S., Gottwald, M., von Savigny, C., Buchwitz, M., Richter, A., Frankenberg, C., Stammes, P., de Graaf, M., Wittrock, F., Sinnhuber, M., Sinnhuber, B. M., Schönhardt, A., Beirle, S., Gloudemans, A., Schrijver, H., Bracher, A., Rozanov, A. V., Weber, M., and Burrows, J. P.: SCIAMACHY's view of the changing Earth's environment, in: SCIAMACHY - Exploring the changing Earth's atmosphere, edited by Gottwald, M. and Bovensmann, H., pp. 175–216, Springer Netherlands, Dordrecht, https://doi.org/10.1007/978-90-481-9896-2_10, 2011.

Bucsela, E., Celarier, E., Wenig, M., Gleason, J., Veefkind, J., Boersma, K., and Brinksma, E.: Algorithm for NO/sub 2/ vertical column retrieval from the ozone monitoring instrument, IEEE Transactions on Geoscience and Remote Sensing, 44, 1245–1258, https://doi.org/10.1109/tgrs.2005.863715, 2006.

Burrows, J. P., Weber, M., Buchwitz, M., Rozanov, V., Ladstätter-Weißenmayer, A., Richter, A., DeBeek, R., Hoogen, R., Bramstedt, K., Eichmann, K.-U., Eisinger, M., and Perner, D.: The Global Ozone Monitoring Experiment (GOME): Mission concept and first scientific results, Journal of the Atmospheric Sciences, 56, 151 – 175, https://doi.org/10.1175/1520-0469(1999)056<0151:TGOMEG>2.0.CO;2, 1999.

Cooper, M. J., Martin, R. V., Hammer, M. S., Levelt, P. F., Veefkind, P., Lamsal, L. N., Krotkov, N. A., Brook, J. R., and McLinden, C. A.: Global fine-scale changes in ambient NO2 during COVID-19 lockdowns, Nature, 601, 380–387, https://doi.org/10.1038/s41586-021-04229-0, 2022.

Crutzen, P. J.: The role of NO and NO2 in the chemistry of the troposphere and stratosphere, Annual review of earth and planetary sciences, 7, 443–472, 1979.

Farrand, W.: Mapping the distribution of mine tailings in the Coeur d'Alene River Valley, Idaho, through the use of a constrained energy minimization technique, Remote Sensing of Environment, 59, 64–76, https://doi.org/10.1016/s0034-4257(96)00080-6, 1997.

Goldin, D., Xiong, X., Shea, Y., and Lukashin, C.: CLARREO Pathfinder/VIIRS Intercalibration: Quantifying the Polarization Effects on Reflectance and the Intercalibration Uncertainty, Remote Sensing, 11, 1914, https://doi.org/10.3390/rs11161914, 2019.

Hollingsworth, A., Engelen, R. J., Textor, C., Benedetti, A., Boucher, O., Chevallier, F., Dethof, A., Elbern, H., Eskes, H., Flemming, J., Granier, C., Kaiser, J. W., Morcrette, J.-J., Rayner, P., Peuch, V.-H., Rouil, L., Schultz, M. G., and and, A. J. S.: TOWARD A MONITORING AND FORECASTING SYSTEM FOR ATMOSPHERIC COMPOSITION, Bulletin of the American Meteorological Society, 89, 1147–1164, https://doi.org/10.1175/2008bams2355.1, 2008.

Huangfu, P. and Atkinson, R.: Long-term exposure to NO2 and O3 and all-cause and respiratory mortality: A systematic review and meta-analysis, Environment International, 144, 105 998, https://doi.org/10.1016/j.envint.2020.105998, 2020.

Joiner, J.: Retrieval of cloud pressure and oceanic chlorophyll content using Raman scattering in GOME ultraviolet spectra, Journal of Geophysical Research, 109, https://doi.org/10.1029/2003jd003698, 2004.

Kim, J., Jeong, U., Ahn, M.-H., Kim, J. H., Park, R. J., Lee, H., Song, C. H., Choi, Y.-S., Lee, K.-H., Yoo, J.-M., Jeong, M.-J., Park, S. K., Lee, K.-M., Song, C.-K., Kim, S.-W., Kim, Y. J., Kim, S.-W., Kim, M., Go, S., Liu, X., Chance, K., Miller, C. C., Al-Saadi, J., Veihelmann, B., Bhartia, P. K., Torres, O., Abad, G. G., Haffner, D. P., Ko, D. H., Lee, S. H., Woo, J.-H., Chong, H., Park, S. S., Nicks, D., Choi, W. J., Moon, K.-J., Cho, A., Yoon, J., kyun Kim, S., Hong, H., Lee, K., Lee, H., Lee, S., Choi, M., Veefkind, P., Levelt, P. F., Edwards, D. P., Kang, M., Eo, M., Bak, J., Baek, K., Kwon, H.-A., Yang, J., Park, J., Han, K. M., Kim, B.-R., Shin, H.-W., Choi, H., Lee, E., Chong, J., Cha, Y., Koo, J.-H., Irie, H., Hayashida, S., Kasai, Y., Kanaya, Y., Liu, C., Lin, J., Crawford, J. H., Carmichael, G. R., Newchurch, M. J., Lefer, B. L., Herman, J. R., Swap, R. J., Lau, A. K. H., Kurosu, T. P., Jaross, G., Ahlers, B., Dobber, M., McElroy, C. T., and Choi, Y.: New Era of Air Quality Monitoring from Space: Geostationary Environment Monitoring Spectrometer (GEMS), Bulletin of the American Meteorological Society, 101, E1–E22, https://doi.org/10.1175/bams-d-18-0013.1, 2020.

Kokaly, R. F., Clark, R. N., Swayze, G. A., Livo, K. E., Hoefen, T. M., Pearson, N. C., Wise, R. A., Benzel, W. M., Lowers, H. A., Driscoll, R. L., and Klein, A. J.: USGS Spectral Library Version 7, https://doi.org/10.3133/ds1035, 2017.

Kolm, M. G., Maurer, R., Sallusti, M., Bagnasco, G., Gulde, S. T., Smith, D. J., and Courrèges-Lacoste, G. B.: Sentinel 4: a geostationary imaging UVN spectrometer for air quality monitoring: status of design, performance and development, in: International Conference on Space Optics — ICSO 2014, edited by Cugny, B., Sodnik, Z., and Karafolas, N., SPIE, https://doi.org/10.1117/12.2304099, 2017.

Kuhlmann, G., Lam, Y. F., Cheung, H. M., Hartl, A., Fung, J. C. H., Chan, P. W., and Wenig, M. O.: Development of a custom OMI NO&ltsub&gt2&lt/sub&gt data product for evaluating biases in a regional chemistry transport model, Atmospheric Chemistry and Physics, 15, 5627–5644, https://doi.org/10.5194/acp-15-5627-2015, 2015.

Lamsal, L. N., Krotkov, N. A., Vasilkov, A., Marchenko, S., Qin, W., Yang, E.-S., Fasnacht, Z., Joiner, J., Choi, S., Haffner, D., Swartz, W. H., Fisher, B., and Bucsela, E.: Ozone Monitoring Instrument (OMI) Aura nitrogen dioxide standard product version 4.0 with improved surface and cloud treatments, Atmos. Meas. Tech., 14, 455–479, https://doi.org/10.5194/amt-14-455-2021, 2021.

Levelt, P., van den Oord, G., Dobber, M., Malkki, A., Visser, H., de Vries, J., Stammes, P., Lundell, J., and Saari, H.: The ozone monitoring instrument, IEEE Transactions on Geoscience and Remote Sensing, 44, 1093–1101, https://doi.org/10.1109/TGRS.2006.872333, 2006.

Levelt, P. F., Joiner, J., Tamminen, J., Veefkind, J. P., Bhartia, P. K., Stein Zweers, D. C., Duncan, B. N., Streets, D. G., Eskes, H., van der A, R., McLinden, C., Fioletov, V., Carn, S., de Laat, J., DeLand, M., Marchenko, S., McPeters, R., Ziemke, J., Fu, D., Liu, X., Pickering, K., Apituley, A., González Abad, G., Arola, A., Boersma, F., Chan Miller, C., Chance, K., de Graaf, M., Hakkarainen, J., Hassinen, S., Ialongo, I., Kleipool, Q., Krotkov, N., Li, C., Lamsal, L., Newman, P., Nowlan, C., Suleiman, R., Tilstra, L. G., Torres, O., Wang, H., and Wargan,

K.: The Ozone Monitoring Instrument: Overview of 14 years in space, Atmos. Chem. Phys., 18, 5699–5745, https://doi.org/10.5194/acp-18-5699-2018, 2018.

370 Marchenko, S., Krotkov, N. A., Lamsal, L. N., Celarier, E. A., Swartz, W. H., and Bucsela, E. J.: Revising the slant column density retrieval of nitrogen dioxide observed by the Ozone Monitoring Instrument, Journal of Geophysical Research: Atmospheres, 120, 5670–5692, https://doi.org/10.1002/2014JD022913, 2015.

Martin, R. V.: An improved retrieval of tropospheric nitrogen dioxide from GOME, Journal of Geophysical Research, 107, https://doi.org/10.1029/2001jd001027, 2002.

375 Meerdink, S. K., Hook, S. J., Roberts, D. A., and Abbott, E. A.: The ECOSTRESS spectral library version 1.0, Remote Sensing of Environment, 230, 111 196, https://doi.org/10.1016/j.rse.2019.05.015, 2019.

Meister, G. and Franz, B. A.: Adjustments to the MODIS Terra radiometric calibration and polarization sensitivity in the 2010 reprocessing, in: Earth Observing Systems XVI, edited by Butler, J. J., Xiong, X., and Gu, X., SPIE, https://doi.org/10.1117/12.891787, 2011.

Molod, A., Takacs, L., Suarez, M., Bacmeister, J., Song, I.-S., and Eichmann, A.: The GEOS-5 atmospheric general circulation model: Mean
380 climate and development from MERRA to Fortuna, Tech. rep., 2012.

Munro, R., Lang, R., Klaes, D., Poli, G., Retscher, C., Lindstrot, R., Huckle, R., Lacan, A., Grzegorski, M., Holdak, A., Kokhanovsky, A., Livschitz, J., and Eisinger, M.: The GOME-2 instrument on the Metop series of satellites: instrument design, calibration, and level 1 data processing – an overview, Atmospheric Measurement Techniques, 9, 1279–1301, https://doi.org/10.5194/amt-9-1279-2016, 2016.

Pearlman, A. J., Cao, C., and Wu, X.: The GOES-R Advanced Baseline Imager: polarization sensitivity and potential impacts, in: Polarization
385 Science and Remote Sensing VII, edited by Shaw, J. A. and LeMaster, D. A., SPIE, https://doi.org/10.1117/12.2188508, 2015.

Richter, A. and Burrows, J.: Tropospheric NO_2 from GOME measurements, Advances in Space Research, 29, 1673–1683, https://doi.org/10.1016/S0273-1177(02)00100-X, 2002.

Shettle, E., Fenn, R., and Laboratory, U. A. F. G.: Models for the Aerosols of the Lower Atmosphere and the Effects of Humidity Variations on Their Optical Properties, AFGL-TR, Air Force Geophysics Laboratory, Air Force Systems Command, United States Air Force, https:
390 //books.google.com/books?id=UoXkXweSrQEC, 1979.

Shindell, D. T., Faluvegi, G., Koch, D. M., Schmidt, G. A., Unger, N., and Bauer, S. E.: Improved attribution of climate forcing to emissions, Science, 326, 716–718, https://doi.org/10.1126/science.1174760, 2009.

Stammes, P., Sneep, M., de Haan, J. F., Veefkind, J. P., Wang, P., and Levelt, P. F.: Effective cloud fractions from the Ozone Monitoring Instrument: Theoretical framework and validation, Journal of Geophysical Research, 113, https://doi.org/10.1029/2007jd008820, 2008.

395 Valks, P., Pinardi, G., Richter, A., Lambert, J.-C., Hao, N., Loyola, D., Van Roozendael, M., and Emmadi, S.: Operational total and tropospheric NO_2 column retrieval for GOME-2, Atmospheric Measurement Techniques, 4, 1491–1514, https://doi.org/10.5194/amt-4-1491-2011, 2011.

Vasilkov, A., Joiner, J., Spurr, R., Bhartia, P. K., Levelt, P., and Stephens, G.: Evaluation of the OMI cloud pressures derived from rotational Raman scattering by comparisons with other satellite data and radiative transfer simulations, Journal of Geophysical Research, 113,
400 https://doi.org/10.1029/2007jd008689, 2008.

Veefkind, J., Aben, I., McMullan, K., Förster, H., de Vries, J., Otter, G., Claas, J., Eskes, H., de Haan, J., Kleipool, Q., van Weele, M., Hasekamp, O., Hoogeveen, R., Landgraf, J., Snel, R., Tol, P., Ingmann, P., Voors, R., Kruizinga, B., Vink, R., Visser, H., and Levelt, P.: TROPOMI on the ESA Sentinel-5 Precursor: A GMES mission for global observations of the atmospheric composition for climate, air quality and ozone layer applications, Remote Sensing of Environment, 120, 70–83, https://doi.org/10.1016/j.rse.2011.09.027, 2012.

405 Voors, R., Bhatti, I. S., Wood, T., Aben, I., Veefkind, P., de Vries, J., Lobb, D., and van der Valk, N.: TROPOMI, the Sentinel 5 precursor instrument for air quality and climate observations: status of the current design, in: International Conference on Space Optics — ICSO 2012, edited by Armandillo, E., Karafolas, N., and Cugny, B., SPIE, https://doi.org/10.1117/12.2309017, 2017.

Wu, A., Geng, X., Wald, A., Angal, A., and Xiong, X.: Assessment of Terra MODIS On-Orbit Polarization Sensitivity Using Pseudoinvariant Desert Sites, IEEE Transactions on Geoscience and Remote Sensing, 55, 4168–4176, https://doi.org/10.1109/tgrs.2017.2689719, 2017.

410 Xu, X. and Wang, J.: UNL-VRTM, A Testbed for Aerosol Remote Sensing: Model Developments and Applications, in: Springer Series in Light Scattering, pp. 1–69, Springer International Publishing, https://doi.org/10.1007/978-3-030-20587-4_1, 2019.

Yan, X., Zang, Z., Zhao, C., and Husi, L.: Understanding global changes in fine-mode aerosols during 2008–2017 using statistical methods and deep learning approach, Environment International, 149, 106 392, https://doi.org/10.1016/j.envint.2021.106392, 2021.

Zoogman, P., Liu, X., Suleiman, R., Pennington, W., Flittner, D., Al-Saadi, J., Hilton, B., Nicks, D., Newchurch, M., Carr, J., Janz, S.,
415 Andraschko, M., Arola, A., Baker, B., Canova, B., Miller, C. C., Cohen, R., Davis, J., Dussault, M., Edwards, D., Fishman, J., Ghulam, A., Abad, G. G., Grutter, M., Herman, J., Houck, J., Jacob, D., Joiner, J., Kerridge, B., Kim, J., Krotkov, N., Lamsal, L., Li, C., Lindfors, A., Martin, R., McElroy, C., McLinden, C., Natraj, V., Neil, D., Nowlan, C., OSullivan, E., Palmer, P., Pierce, R., Pippin, M., Saiz-Lopez, A., Spurr, R., Szykman, J., Torres, O., Veefkind, J., Veihelmann, B., Wang, H., Wang, J., and Chance, K.: Tropospheric emissions: Monitoring of pollution (TEMPO), Journal of Quantitative Spectroscopy and Radiative Transfer, 186, 17–39,
420 https://doi.org/10.1016/j.jqsrt.2016.05.008, 2017.